Discover Oncology

Research

The integrated single-cell analysis interpret the lactate metabolism-driven immune suppression in triple-negative breast cancer

Xinhai Gao[1] · Tianhua Wang[1] · Cun Liu[2] · Ye Li[1] · Wenfeng Zhang[2] · Minpu Zhang[1] · Yan Yao[3] · Chundi Gao[2] · Ruijuan Liu[3] · Changgang Sun[2,3]

Received: 28 January 2025 / Accepted: 6 May 2025
Published online: 16 May 2025

Abstract

Background Individuals with triple-negative breast cancer (TNBC) exhibit elevated lactate levels, which offers a valuable lead for investigating the molecular mechanisms underlying the tumor microenvironment (TME) and identifying more efficacious treatments.

Methods TNBC samples were classified based on lactate-associated genes. A single-cell transcriptomic approach was employed to examine functional differences across cells with varying lactate metabolism. Immunohistochemistry was used to explore the relationship between lactate metabolism and the CXCL12/CXCR4 signaling axis. In addition, utilizing machine learning techniques, we constructed a prognostic model based on lactic acid phenotype genes.

Results Lactate-associated gene-based stratification revealed increased immune cell infiltration and immune checkpoint expression in Lactate Cluster 1. Elevated lactate metabolism scores were observed in both cancer-associated fibroblasts (CAFs) and malignant cells. CAFs with high lactate metabolism exhibited immune suppression through the CXCL12/CXCR4 axis. Immunohistochemistry confirmed elevated LDHA, LDHB, CXCL12, and CXCR4 levels in the high lactate group.

Conclusion This study elucidates the complex interplay between lactate and immune cells in TNBC and highlights the CXCL12/CXCR4 axis as a key pathway through which lactate mediates immune suppression, offering new insights into metabolic regulation within the TME. Furthermore, we developed a prognostic model based on lactate metabolism phenotype genes to predict the prognosis of TNBC patients and guide immunotherapy.

Keywords Triple-negative breast cancer · Lactate · Tumor microenvironment

Supplementary Information The online version contains supplementary material available at https://doi.org/10.1007/s12672-025-02605-0.

✉ Changgang Sun, scgdoctor@126.com | [1]Faculty of Chinese Medicine and State Key Laboratory of Quality Research in Chinese Medicines, Macau University of Science and Technology, Macao 999078, Macao, China. [2]College of Traditional Chinese Medicine, Shandong Second Medical University, 261000, Weifang, Shandong, China. [3]Department of Oncology, Weifang Traditional Chinese Hospital, Weifang 261000, Shandong, China.

1 Introduction

Breast cancer remains the most widespread malignancy affecting women globally and is the second leading cause of cancer-related deaths worldwide [1]. Based on hormone receptor (HR) expression and *HER2* gene amplification, breast cancer is classified into hormone receptor-positive, HER2-overexpressing, and triple-negative breast cancer (TNBC) [2]. Among these subtypes, TNBC exhibits increased aggressiveness, early metastatic tendency, and elevated recurrence and mortality rates [3]. The absence of relevant receptors prevents patients with TNBC from benefiting from endocrine- or HER2-targeted therapies [4]. Consequently, chemotherapy is the primary non-surgical approach for TNBC therapy, albeit with limited efficacy, as < 30% of patients achieve complete remission post-treatment [5]. Recently, the emergence of immunotherapy has sparked hope in the therapeutic landscape of TNBC; however, it still faces considerable challenges [6]. A thorough exploration of the complex characteristics of the tumor microenvironment (TME) in TNBC serves as a vital foundation for TNBC immunotherapy.

The TME is known for its remarkable complexity and heterogeneity [7]. A key hallmark of cancer is its ability to suppress the immune system, allowing cancer cells to evade immune surveillance [8]. Cancer cells, characterized by metabolic abnormalities, ravenously devour copious amounts of oxygen [9]. Such consumption leads to hypoxia, nutritional deficiencies, and accumulation of metabolic by-products within the TME [10]. Importantly, the build-up of these metabolites, particularly lactic acid, substantially contributes to the creation of an immunosuppressive environment that favors cancer cell proliferation and immune evasion [11].

Lactic acid has traditionally been regarded as a metabolic waste product. However, in the 1920s, the discovery of aerobic glycolysis revealed considerable metabolic differences between tumors and healthy tissues, highlighting a distinctive role in tumor biology [12]. Aerobic glycolysis, often referred to as the Warburg effect, is a characteristic feature of cancer cells [13]. This signifies the tendency of malignant cells to generate energy via glycolysis as opposed to oxidative phosphorylation, even in an oxygen-rich environment [14]. This preference ultimately leads to abnormally high lactic acid concentrations in tumor tissues [15]. Research advancements have revealed that lactic acid is not only an energy-rich signaling molecule, but also exhibits unique biological functions [16]. It is closely associated with tumor invasion, metastasis, angiogenesis, and immune evasion [17, 18]. Within the complex TME, lactic acid circulates among various cell types, facilitating cancer progression by modulating cellular immune responses [19]. Compared to other cancers, TNBC cells exhibit a remarkably elevated level of glycolysis [20] and a substantially higher concentration of lactic acid in tumors [21]. Exploring the role of lactic acid in the TME may provide profound insights into the molecular mechanisms underlying TNBC pathogenesis and paves the way for more effective therapies.

In this comprehensive study, we utilized single-cell RNA sequencing (scRNA-seq) and bulk RNA sequencing (bulk RNA-seq) to explore the intricate interactions between lactate-related genes and lactate phenotype genes in the pathogenesis and progression of TNBC. We developed a lactic acid-related model that accurately reflects lactic acid levels within a single-cell transcriptome, providing a deeper understanding of the metabolic landscape in TNBC. Through detailed analysis of the differential expression of lactate-related phenotypic genes across various TNBC cell types at the single-cell level, we identified potential signaling pathways through which lactate may modulate cellular immunity within the TME. To further validate our hypothesis, we established a murine model of TNBC. Immunohistochemical analysis revealed that the high lactate metabolism group exhibited upregulation of LDHA, LDHB, CXCL12, and CXCR4. This finding validates the expression of the lactate metabolism-driven CXCL12/CXCR4 signaling axis in TNBC, highlighting the crucial role of lactate metabolism in promoting immune suppression within the TME. In addition, we developed a prognostic model focused on lactate metabolism phenotype genes, validated using public databases. This model can accurately predict the prognosis of TNBC patients and offer valuable guidance for the implementation of immunotherapy, facilitating more targeted and effective treatment strategies.

2 Materials and methods

2.1 Selection of lactate-related genes

From the previous literature [22–27] and the KEGG database, we identified 210 lactate-related genes, which are listed in Supplementary Material 1.

2.2 Patients and samples

Public datasets used in this study were obtained from The Cancer Genome Atlas (TCGA, http://cancergenome.nih.gov/) and the Gene Expression Omnibus (GEO, http://www.ncbi.nlm.nih.gov/geo/). We collected six independent public datasets related to TNBC patients. Among these, two datasets (TCGA-BRCA and GSE58812) provided comprehensive overall survival (OS) and gene expression profiling data, which were instrumental in developing and validating our features. The remaining three datasets (GSE18864, GSE76124, and GSE83937) included only gene expression profiling data, which were used to assess the predictive efficacy of the gene signature in immunotherapy. Additionally, the scRNA-seq data used in our study were derived from the GSE176078 dataset, which included information from nine TNBC patients.

All patients included in the study were diagnosed with TNBC, characterized by the absence of estrogen receptor, progesterone receptor, and human epidermal growth factor receptor 2 expression. All patients included in the study were female, with ages primarily ranging from 20 to 80 years. The tumor staging predominantly consisted of stages I to III, with the majority of tumors classified as T1 to T3. In terms of nodal involvement, the N staging was mainly concentrated in N0 to N2, while most patients were classified as M0, indicating no distant metastasis.

2.3 Determination of lactate-related gene clusters

Consensus clustering based on the expression of lactate-related genes was performed using the ConsensusClusterPlus package in R [28]. The distance metric employed was based on Pearson's correlation, and Hierarchical Clustering was used as the clustering methodology. To ascertain stability of the classification, 500 repeated samples were analyzed [29].

The clustering process gave rise to two distinct lactate clusters, namely Lactate Cluster 1 (LC1) and Lactate Cluster 2 (LC2). Differentially expressed genes (DEGs) between these clusters were identified based on the criteria of absolute $\log_2 FC >= 1$ and adjusted P-value < 0.05. A comprehensive list of these DEGs is presented in Supplementary Material 2.

2.4 Estimation of immune cell infiltration

The immune, stromal, and tumor fractions within each sample were estimated using the ESTIMATE package in R [30]. The results were quantified as Immune Score, Stromal Score, Tumor Purity, and ESTIMATE Score. Specifically, the immune and stromal scores were positively correlated with the abundance of immune and stromal cells, respectively, whereas Tumor Purity reflected the proportion of tumor cells. The ESTIMATE Score represents the sum of the Immune and Stromal Scores.

Furthermore, we analyzed the samples for the extent of immune cell infiltration using the GSVA algorithm (selection of ssGSEA methodology) from the GSVA package in R [31]. The scores obtained for each immune cell type within the samples were directly proportional to the level of infiltration by specific immune cells.

2.5 Enrichment analysis

Gene ontology (GO), KEGG, and GSEA analyses were conducted utilizing enrichGO, enrichKEGG, and GSEA algorithms provided by the clusterProfiler package in R [32]. These offered profound insights into the classification of gene functions and the enrichment of biological pathways, which were considered significantly enriched only if their P-values were < 0.05.

2.6 Preprocessing and analysis of scRNA-seq data

2.6.1 Data pre-processing, filteration, and normalization

The scRNA-seq dataset was processed using Seurat v4 [33]. We pre-selected cells expressing between 50 and 4000 genes and having < 20,000 UMIs(Unique Molecular Identifiers) based on their respective expression profiles. The filtering criteria encompassed a mitochondrial gene fraction < 20%. Data normalization was achieved using Seurat's normalizeData function with a scale factor of 10,000. To identify the most variable DEGs, we employed the FindVariableFeatures

function and selected the top-2000 genes for subsequent analyses. Subsequently, the ScaleData function was used to adjust gene expression levels.

2.6.2 Clustering and cell-type annotation

Principal component analysis (PCA)-based linear dimensionality reduction was applied to the scaled dataset using the RUNPCA function. Following this, data integration was conducted on Seurat objects via the IntegrateLayers function, specifically for the HarmonyIntegration method. By selecting 30 principal components, Shared Nearest Neighbor (KNN) graphs and Unified Flow Approximation and Projection (UMAP) maps were generated using Louvain's clustering algorithm. The FindAllMarkers function facilitated the identification of DEGs. Cellular annotations for this study were sourced from the Tumor Immune Single Cell Hub 2 (TISCH2, http://tisch.compgenomics.org) [34].

2.7 Calculation of lactate score

To investigate lactate levels in individual cells or samples, we employed an algorithm that assesses variations in the signal-to-noise ratio among genes and cells [35], utilizing the expression profiles of lactate-associated genes. This approach enabled us to estimate lactate levels within a specific cell or sample (Supplementary Material 3).

The median LPGs (lactate phenotype genes) score served as the threshold for classifying cells into LPGs-high and LPGs-low clusters.

2.8 Pseudo-temporal analysis

Pseudo-temporal analyses were conducted using the Monocle 3 package [36]. Initially, pseudo-temporal objects were constructed and genes expressed in a minimum of 5% of cells were chosen. Subsequently, size factors and dispersion were calculated for each cell and low-quality cells were excluded (with a minimum gene expression threshold of 0.1). Following the selection of highly variable genes, dimensionality reduction analysis was performed using the ReduceDimension function. Finally, the orderCells function was used to organize cells along quasitemporal trajectories.

2.9 Cell–cell communication

To further investigate and examine intercellular communication, we employed the CellChat package, referencing the CellChatDB human database, to identify proteins with high expression levels and ligand-receptor pairs [37]. Subsequently, we inferred communication networks and computed the outcomes of all ligand-receptor interactions linked to individual signaling pathways.

2.10 Murine tumor models

Six-week-old female Balb/c mice were purchased from Beijing Vital River Laboratory Animal Technology Co., Ltd. and housed under specific pathogen-free conditions (21–23 °C, 35–55% humidity, 12-h light–dark cycle). Mice were used for experiments between 5 and 10 weeks of age, with tumor diameters not exceeding 20 mm. All procedures were approved by the Ethics Committee of Shandong Second Medical University.

The 4T1-luc murine breast cancer cell line (Shanghai Yizefeng Biotechnology) and the L929 murine fibroblast cell line (Wuhan Punose Life Science Technology) were cultured in DMEM with 10% FBS. To induce cancer-associated fibroblast (CAF) transformation, L929 cells were treated with 10 ng/ml TGF-β1 for 48 h, upregulating α-SMA expression. For tumor implantation, both cell lines were trypsinized, centrifuged, washed, and resuspended to a density of 5 × 10^6 cells/ml before subcutaneous injection into the axillae of mice. The control group received 4T1-luc cells alone. Tumor size and general health were monitored, and after three weeks, mice were euthanized and tumors collected for immunohistochemistry [38].

2.10.1 Immunohistochemistry

The α-SMA (Cat No. 14395–1-AP;Concentration:1:3000), LDHA (Cat No. 19987–1-AP;Concentration:1:200), LDHB (Cat No. 14824–1-AP;Concentration:1:1400),CXCL12 (Cat No. 17402–1-AP;Concentration:1:500) and CXCR4(Cat No. 11073–2

-AP;Concentration:1:500) antibodies were purchased from Proteintech Group (Wuhan SaiYing Biotechnology Co., Ltd.). Follow the staining procedure outlined in the kit's manual with strict adherence to ensure precise execution of the specificity staining conditions.

Tumor tissues were fixed in formalin, embedded in paraffin, and sectioned (4 μm). Deparaffinization was performed in Eco-friendly Xylene Solutions I-III (10 min each) followed by ethanol washes and distilled water rinsing. Endogenous peroxidase activity was quenched with 3% hydrogen peroxide for 25 min, followed by PBS washes. Sections were blocked with 3% BSA for 30 min, then incubated with primary antibodies overnight at 4 °C. After washing, HRP-conjugated secondary antibodies were applied for 50 min at room temperature.

DAB chromogenic solution was used to visualize positive signals, with the reaction stopped when brown–yellow staining appeared. Sections were counterstained with hematoxylin, differentiated, and dehydrated through ethanol and *n*-butanol solutions. After clearing in xylene, sections were mounted with coverslips and evaluated under a light microscope. Hematoxylin stained cell nuclei blue, and DAB staining appeared brown–yellow.The expression levels of the studied markers were quantified using ImageJ software following immunohistochemistry. The positive area percentage was calculated as a reference for the expression level of each marker.

2.11 Weighted correlation network analysis (WGCNA)

The WGCNA package was used to establish gene co-expression networks [39]. A suitable soft threshold adhering to the scale-free network criterion was computed. Based on this threshold, a weighted neighbor matrix was converted into a topological overlap matrix (TOM), which then generated corresponding dissimilarity measure (1-TOM). Modules were identified using the dynamic tree-cutting method. To identify gene modules significantly linked to immune clusters, we selected those modules that exhibited the strongest correlation for further investigation.

2.12 Signature generated from machine learning-based integrative approaches

To devise a highly accurate and stable lactate-related risk signature, we amalgamated 10 machine learning algorithms with 101 algorithm combinations [40]. The integrative algorithms including random survival forest, elastic network, Lasso, Ridge, stepwise Cox, CoxBoost, partial least squares regression for Cox, supervised principal components, generalized boosted regression modelling, and survival support vector machine.

The signature generation procedure was as follows: (a) Univariate Cox regression identified prognostic genes in the TCGA cohort; (b) Then, 101 algorithm combinations were performed on the prognostic genes to fit prediction models based on the leave-one-out cross-validation (LOOCV) framework in the TCGA cohort; (c) All models were detected in validation data set (GSE58812); (d) For each model, Harrell's concordance index (C-index) was calculated across two datasets, and the model with the highest average C-index was considered optimal.

2.13 Statistical analysis

All data processing, statistical analysis, and graphing were performed using R4.3.3 software. The overall survival of patients in high- and low-risk groups was compared via the Kaplan–Meier analysis with the log-rank test. Wilcoxon test was performed to ascertain the gene expression levels between two groups and assess the variance in immune scores between the two risk groups. All p values two-tailed with $p < 0.05$ in single tests and adjusted $p < 0.05$ in multiple tests were considered statistically significant. Each analysis was systematically repeated to ensure the reliability of the results.

3 Results

3.1 Defining lactate-related classes of triple-negative breast cancer (TNBC)

Tumor samples from 154 patients with TNBC in the TCGA-BRCA dataset were grouped based on lactate gene expression patterns. A consensus-clustering methodology was employed to classify the samples into distinct groups. A thorough examination of covariance correlation coefficients was conducted, leading to the selection of an optimal cluster count of 2. The consensus matrix heatmap remained clear and well-defined at $k = 2$ (Fig. 1A, B), indicating that sample the

Fig. 1 Identification of lactate phenotype genes. **A** Consensus score matrix of all samples when k = 2. A higher consensus score between two samples indicates that they are more likely to be grouped into the same cluster in different iterations. **B** CDF curves of consensus matrix for each k (indicated by colors).**C** Boxplot of ESTIMATE scores in LC1 and LC2. **D** Boxplot of immune cell population abundance in LC1 and LC2 groups. **E** Boxplot of expression of immune checkpoint genes in LC1 and LC2 groups. **F** Volcano plot of DEGs between LC1 and LC2. **G** Heat map of TOP50 genes of DEGs between LC1 and LC2 groups. **H** GO analysis of LPGs. **I** KEGG analysis of LPGs. **J** GSEA analysis of LPGs

clustering procedure was robust and reliable. Our findings revealed that patients can be neatly segmented into two lactate clusters, designated as LC1 and LC2.

Next, we investigated predictive values of the two clusters. The 2 lactate clusters were analyzed using ESTIMATE and ssGSEA. Our findings revealed that the StromalScore ($P < 0.01$), ImmuneScore ($P < 0.001$), and ESTIMATEScore ($P < 0.001$) were notably elevated in LC1 compared to LC2 (Fig. 1C). ssGSEA indicated that LC1 exhibited higher infiltration levels by various immune cell types, including B cells, T cells, mast cells, natural killer cells, and MDSCs than LC2. Furthermore, we examined disparities in the expression of immune checkpoint markers between the two lactate clusters (Fig. 1D). The results demonstrated that several immune checkpoint markers, including PDCD1 (PD-1), CD274 (PD-L1), PDCD1LG2 (PD-L2), CTLA4, and others, were significantly upregulated in LC1 compared to LC2 ($P < 0.001$) (Fig. 1E). These findings indicate that patients belonging to the LC1 cluster possess tumor tissues characterized by a higher degree of immune cell infiltration, accompanied by a more intricate cellular immune response.

3.2 Description of lactate phenotype genes (LPGs)

To enhance the characterization of lactate-related phenotypes in TNBC, we conducted a differential analysis of lactate clusters. Using threshold criteria where the absolute $\log_2$FC was greater than or equal to 1 and the adjusted *P*-value was < 0.05, we identified 1,187 genes (Fig. 1F, G). These genes were designated LPGs.

Subsequently, we performed GO, KEGG, and GSEA analyses on these LPGs. GO analysis revealed that these genes were highly enriched in immune-related biological processes, such as the 'regulation of T cell activation,' 'mononuclear cell differentiation,' and 'leukocyte-mediated immunity.' Additionally, they were enriched in molecular functions linked to 'cytokine activity,' 'carbohydrate binding,' and 'immune receptor activity,' indicating their roles in immune and metabolic processes (Fig. 1H).

KEGG analysis demonstrated that the LPGs were predominantly enriched in the 'cytokine–cytokine receptor interaction' pathway (Fig. 1I). Furthermore, results of GSEA analysis provided 16 HALLMARK gene sets, primarily focused on cellular immunity ('interferon gamma response,' 'interferon alpha response,' 'IL2-STAT5 signaling,' 'TNF-α signaling via NF-κB') and lactate glycolysis (e.g., 'glycolysis, ' 'hypoxia, ' 'oxidative phosphorylation') (Fig. 1J). Furthermore, the LPGs exhibited significant enrichment in the "MYC target" gene set, which is intimately associated with glucose metabolism in TNBC [41, 42].

3.3 Identifying LPGs in TNBC from single-cell transcriptome data

To evaluate the importance of LPGs at single-cell resolution, we incorporated the GSE176078 dataset using the Seurat package. From this integrated dataset, we selected samples from nine patients with TNBC.

Following gene expression normalization, we conducted PCA and clustered the cells within the informative PCA space by employing UMAP-based clustering. This approach led to the identification of 16 distinct cell clusters characterized by DEGs (Fig. 2A). Using genetic markers, we classified these cell populations into recognized cell lineages, including CD8 + T cells, malignant cells, mono/macrocells, CD4 + T cells, cancer-associated fibroblasts (CAFs), plasma cells, B cells, smooth muscle cells (SMCs), endothelial cells, proliferating T cells (Tprolif), and dendritic cells (DCs) (Fig. 2B).

We subsequently devised scoring algorithms to calculate LPGs scores for individual TNBC cells. As demonstrated, LPGs scores exhibited notable variation among the different cell populations (Fig. 2C). The cells with high LPGs scores were primarily CAFs, malignant cells, SMCs, and endothelial cells, whereas only a few CD8 + T cells, CD4 + T cells, B cells, and DCs had high LPGs scores (Fig. 2D). This finding aligns with previous studies indicating that within the TME, lactate is predominantly generated by CAFs and malignant cells [43, 44].

Furthermore, we stratified CAFs and malignant cells into high and low groups based on their LPGs scores to investigate differences at the single-cell level. The CAFs were evenly divided into CAF-high and CAF-low subgroups according to their LPG scores. Similarly, malignant cells were categorized into malignant-high and malignant-low subgroups.

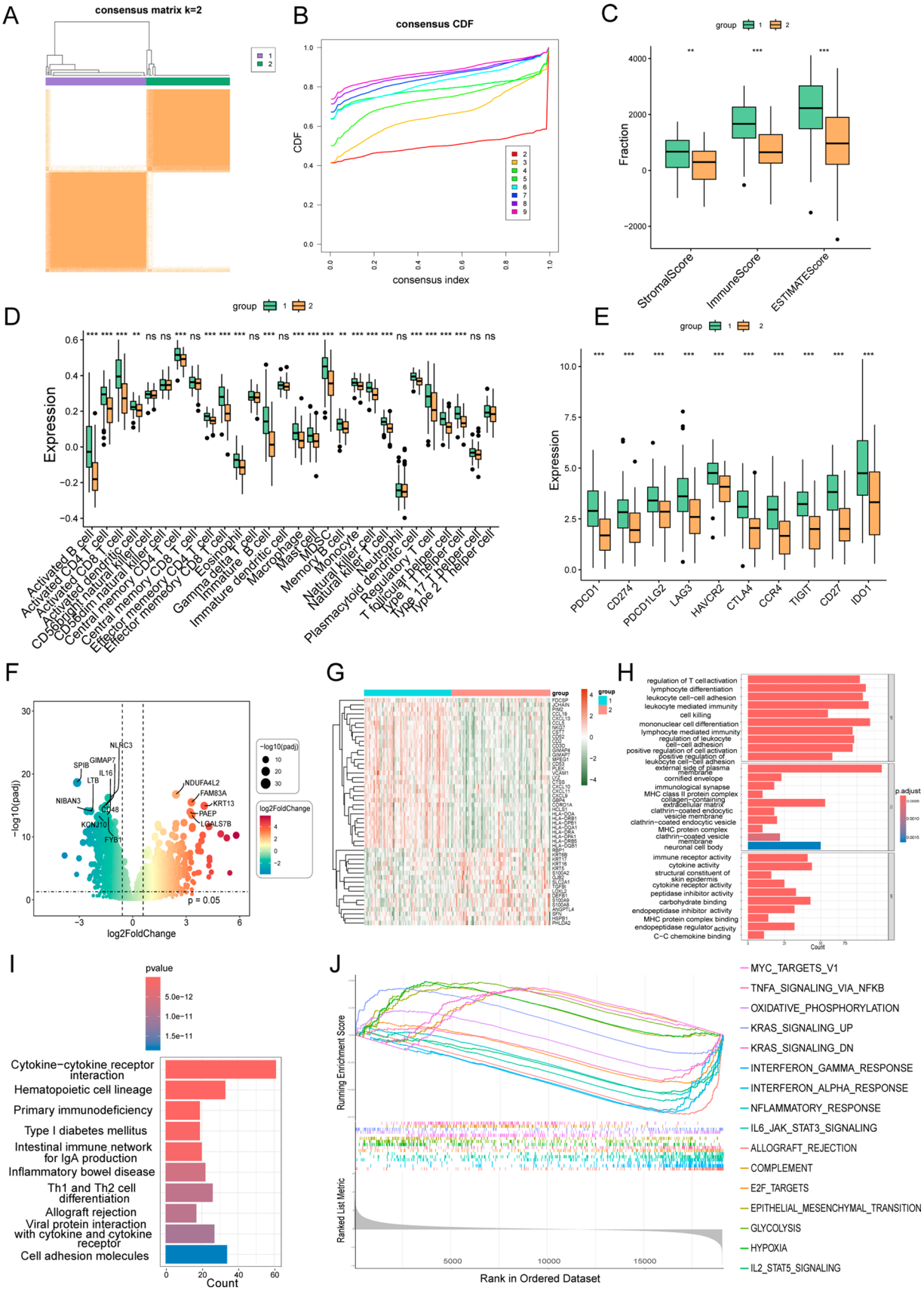
A
consensus matrix k=2
B
consensus CDF
CDF
consensus index
C
group 1 2
Fraction
StromalScore
ImmuneScore
ESTIMATEScore
D
group 1 2
Expression
Activated B cell
Activated CD4 T cell
Activated CD8 T cell
Activated dendritic cell
CD56bright natural killer cell
CD56dim natural killer cell
Central memory CD4 T cell
Central memory CD8 T cell
Effector memeory CD4 T cell
Effector memeory CD8 T cell
Eosinophil
Gamma delta T cell
Immature B cell
Immature dendritic cell
Macrophage
Mast cell
MDSC
Memory B cell
Monocyte
Natural killer cell
Natural killer T cell
Neutrophil
Plasmacytoid dendritic cell
Regulatory T cell
T follicular helper cell
Type 1 T helper cell
Type 17 T helper cell
Type 2 T helper cell
E
group 1 2
Expression
PDCD1
CD274
PDCD1LG2
LAG3
HAVCR2
CTLA4
CCR4
TIGIT
CD27
IDO1
F
−log10(padj)
log2FoldChange
NLRC3
SPIB
GIMAP7
IL16
LTB
NIBAN3
CD48
KCNJ10
FYB1
NDUFA4L2
FAM83A
KRT13
PAEP
LGALS7B
p = 0.05
G
group 1 2
H
regulation of T cell activation
lymphocyte differentiation
leukocyte cell−cell adhesion
leukocyte mediated immunity
cell killing
mononuclear cell differentiation
lymphocyte mediated immunity
regulation of leukocyte cell−cell adhesion
positive regulation of cell activation
positive regulation of leukocyte cell−cell adhesion
external side of plasma membrane
cornified envelope
immunological synapse
MHC class II protein complex
collagen−containing extracellular matrix
clathrin−coated endocytic vesicle membrane
clathrin−coated endocytic vesicle
MHC protein complex
clathrin−coated vesicle membrane
neuronal cell body
immune receptor activity
cytokine activity
structural constituent of skin epidermis
cytokine receptor activity
peptidase inhibitor activity
carbohydrate binding
endopeptidase inhibitor activity
MHC protein complex binding
endopeptidase regulator activity
C−C chemokine binding
p.adjust
Count
I
pvalue
Cytokine−cytokine receptor interaction
Hematopoietic cell lineage
Primary immunodeficiency
Type I diabetes mellitus
Intestinal immune network for IgA production
Inflammatory bowel disease
Th1 and Th2 cell differentiation
Allograft rejection
Viral protein interaction with cytokine and cytokine receptor
Cell adhesion molecules
Count
J
Running Enrichment Score
Ranked List Metric
Rank in Ordered Dataset
MYC_TARGETS_V1
TNFA_SIGNALING_VIA_NFKB
OXIDATIVE_PHOSPHORYLATION
KRAS_SIGNALING_UP
KRAS_SIGNALING_DN
INTERFERON_GAMMA_RESPONSE
INTERFERON_ALPHA_RESPONSE
NFLAMMATORY_RESPONSE
IL6_JAK_STAT3_SIGNALING
ALLOGRAFT_REJECTION
COMPLEMENT
E2F_TARGETS
EPITHELIAL_MESENCHYMAL_TRANSITION
GLYCOLYSIS
HYPOXIA
IL2_STAT5_SIGNALING

Fig. 2 LPGs score heterogeneity is found across different cells in TNBC. **A** Umap plot colored by various cell clusters. **B** Cell type identified by ▶ marker genes. **C** Cells are colored in terms of LPGs scores. **D** Relative proportion of LPGs-high cells across 11 clusters. **E** GO analysis of marker genes in CAFs. **F** GO analysis of marker genes in malignant cells

We initially conducted enrichment analysis for marker genes in CAFs and malignant cells. Gene ontology (GO) analysis revealed that CAFs with low LPGs scores exhibited greater enrichment in terms of 'aerobic respiration', 'mitochondrial gene expression,' and 'mitochondrial translation' (Fig. 2E). This indicated that CAFs with low LPGs scores predominantly rely on mitochondrial oxidative phosphorylation for their metabolic activities. Similarly, marker genes in malignant cells with low LPGs scores were enriched in 'mitochondrial gene expression' (Fig. 2F), further highlighting the ability of our LPGs score to differentiate between cellular metabolic modes. To a certain degree, the LPGs score was inversely correlated with aerobic respiratory capacity of the cell. Cells with high LPGs score preferentially utilize glycolysis as their energy source, resulting in increased lactic acid production.

To explore potential evolutionary relationships between cells with high and low LPGs scores, we employed the Monocle tool to uncover the postulated temporal sequences of cell clusters analogous to developmental lineages. This analysis revealed a dynamic evolutionary trajectory from cells with low to high LPGs scores within the CAF population (Fig. 3A–C). Previous research has documented a notable shift in CAF metabolism from oxidative phosphorylation to aerobic glycolysis compared to normal fibroblasts. Our pseudo-temporal analysis findings align with this observation and provide further evidence supporting this metabolic transition. Moreover, a comparable trend was detected in malignant cells, indicating that tumor cells undergo continuous metabolic reprogramming as cancer progresses (Fig. 3D–F).

Cell Chat illuminates disparities in intercellular communication between cell populations characterized by high and low LPGs scores. Within the malignant cell population, the high-scoring subset demonstrated heightened signaling capacity involving pathways such as MIF (Macrophage Migration Inhibitory Factor), VEGF, and MK(Midkine), compared to the low-scoring cohort (Fig. 4A–G). For instance, endothelial cells serve as targets and are modulated by high-malignancy cells via the VEGF pathway (Fig. 4C, E). This distinction suggests a potential association between lactate and tumor-induced angiogenesis.

Among the CAFs, those with high LPGs scores exhibited greater significance in multiple signaling pathways and demonstrated closer interactions with immune cells, including CD8 T, CD4 T, B, and mono/macro cells (Figs. 4H–N). Specifically, CAFs with high scores engaged more actively in the functional modulation of CD8T, CD4T, and B cells through the CXCL pathway, particularly via the CXCL12/CXCR4(C-X-C Chemokine Receptor Type 4) signaling axis, compared to their low-scoring counterparts (Fig. 4J, M). Furthermore, these high-scoring CAFs, which predominantly expressed EGFR receptors, exhibited increased sensitivity to EGF signaling, thereby enhancing their proliferation and migration capabilities (Fig. 4K).

3.4 The CXCL12/CXCR4 pathway is a key mediator of lactate metabolism-induced immune suppression

To further investigate the relationship between lactate metabolism and immune cell function, we established a mouse model associated with lactate metabolism. Immunohistochemical analysis was employed to examine the impact of lactate metabolism on the expression of the CXCL12/CXCR4 pathway in CAFs. The results indicated that, compared to the control group, the experimental group exhibited a significantly increased expression of α-SMA, suggesting robust CAF proliferation (Fig. 5A).

Additionally, the experimental group showed a marked upregulation of LDHA and LDHB expression, indicating elevated lactate metabolism in these mice (Fig. 5A). This finding supports previous literature suggesting that CAFs enhance lactate metabolism [8, 45]. Notably, the experimental group also exhibited higher expression levels of CXCL12 and CXCR4 (Fig. 5A). Quantitative analysis of immunohistochemical results confirmed these observations, with statistically significant differences (Fig. 5B). These findings collectively suggest that enhanced lactate metabolism in TNBC promotes the expression of the CXCL12/CXCR4 pathway.

3.5 Identification of gene modules derived from immune infiltration patterns

In our study, we identified significant differences in immune cell infiltration and immune checkpoint markers between subtypes LC1 and LC2, with notable enrichment of lactate phenotype genes (LPGs) in cellular immunity. Single-cell analysis and immunohistochemistry further confirmed the role of lactate phenotype genes in modulating cellular immunity. Recognizing the compelling need to investigate the interplay between LPGs and tumor immunity, we employed WGCNA to scrutinize these genes and extract immune-related gene modules.

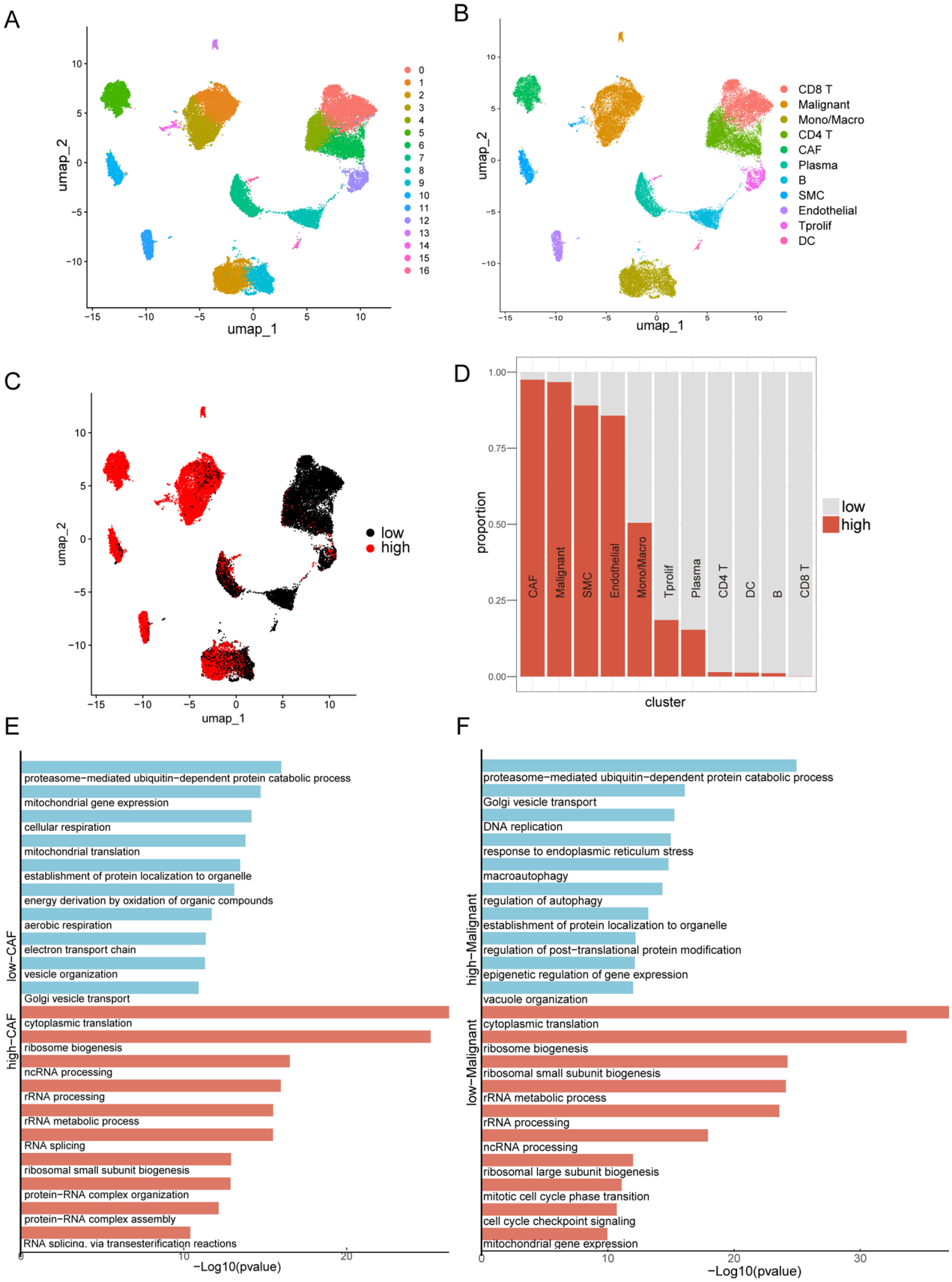
A
umap_2
umap_1
0
1
2
3
4
5
6
7
8
9
10
11
12
13
14
15
16
B
umap_2
umap_1
CD8 T
Malignant
Mono/Macro
CD4 T
CAF
Plasma
B
SMC
Endothelial
Tprolif
DC
C
umap_2
umap_1
low
high
D
proportion
cluster
CAF
Malignant
SMC
Endothelial
Mono/Macro
Tprolif
Plasma
CD4 T
DC
B
CD8 T
low
high
E
low−CAF
high−CAF
proteasome−mediated ubiquitin−dependent protein catabolic process
mitochondrial gene expression
cellular respiration
mitochondrial translation
establishment of protein localization to organelle
energy derivation by oxidation of organic compounds
aerobic respiration
electron transport chain
vesicle organization
Golgi vesicle transport
cytoplasmic translation
ribosome biogenesis
ncRNA processing
rRNA processing
rRNA metabolic process
RNA splicing
ribosomal small subunit biogenesis
protein−RNA complex organization
protein−RNA complex assembly
RNA splicing, via transesterification reactions
−Log10(pvalue)
F
high−Malignant
low−Malignant
proteasome−mediated ubiquitin−dependent protein catabolic process
Golgi vesicle transport
DNA replication
response to endoplasmic reticulum stress
macroautophagy
regulation of autophagy
establishment of protein localization to organelle
regulation of post−translational protein modification
epigenetic regulation of gene expression
vacuole organization
cytoplasmic translation
ribosome biogenesis
ribosomal small subunit biogenesis
rRNA metabolic process
rRNA processing
ncRNA processing
ribosomal large subunit biogenesis
mitotic cell cycle phase transition
cell cycle checkpoint signaling
mitochondrial gene expression
−Log10(pvalue)

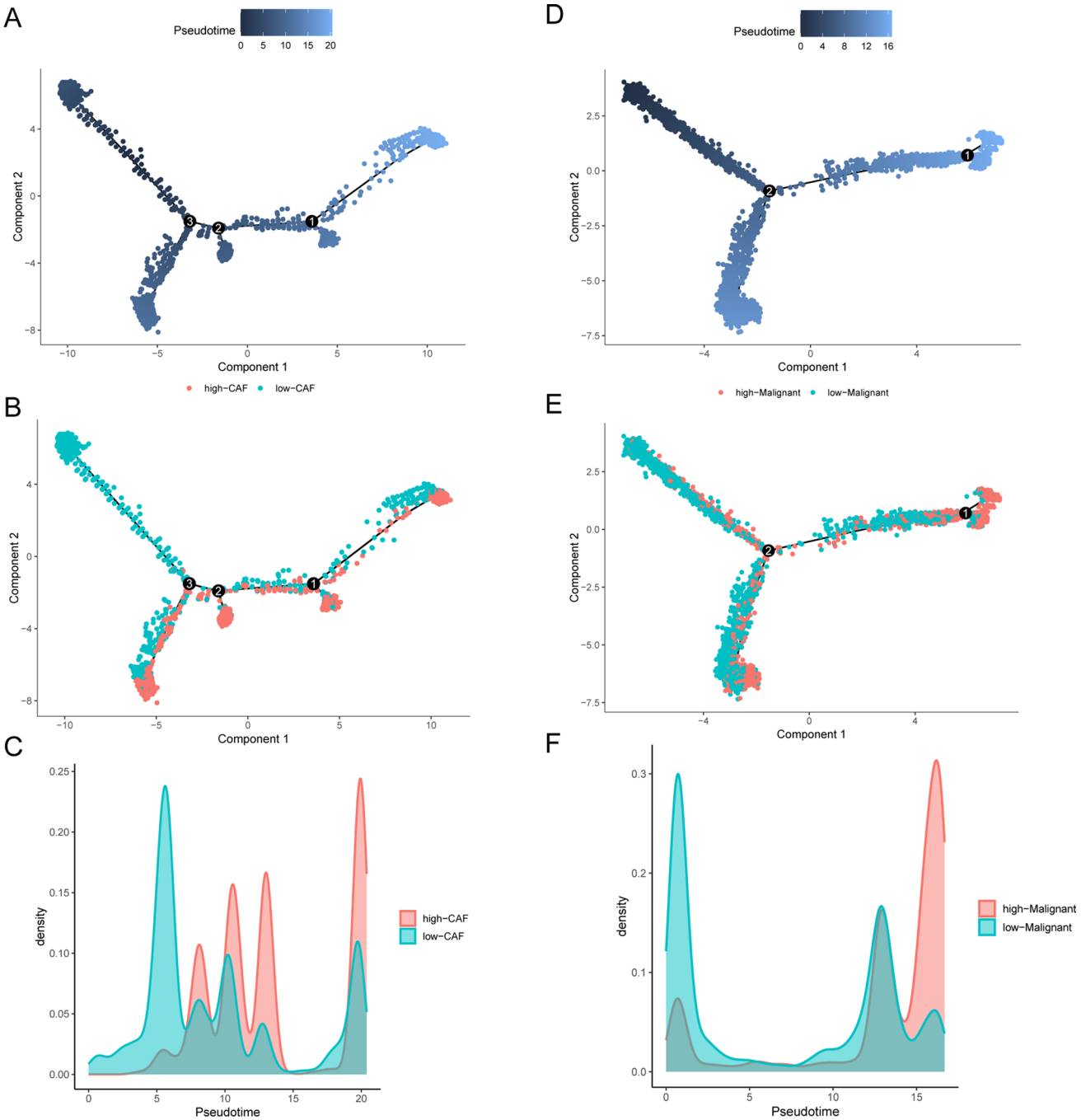

Fig. 3 Pseudo-temporal analysis of different LPGs scored CAFs and Malignant. **A** Trajectory diagram of cell differentiation time for high- CAF and low-CAF. **B** Trajectory diagram of high- CAF and low-CAF. **C** Plot of cell density along the timeline for high- CAF and low-CAF. **D** Trajectory diagram of cell differentiation time for high- Malignant and low-Malignant. **E** Trajectory diagram of high- Malignant and low-Malignant. F Plot of cell density along the timeline for high-Malignant and low-Malignant

For conducting WGCNA, we adjusted the soft threshold β to 9 (achieving a scale-free R2 of 0.921), providing an optimal power value for constructing robust co-expression networks (Fig. S1A). Subsequently, we delineated eight distinct gene modules, each represented by a unique color (Fig. S1B) and quantified correlations using ESTIMATE. Among these module-trait associations, the purple module exhibited the strongest correlation with immunization scores (Fig. S1C). Notably, within the purple module, the correlation coefficient between gene significance (GS) and module membership (MM) was 0.97, indicating excellent quality of the constructed gene modules (Fig. S1D). We identified 324 genes with a GS > 0.5 and a MM > 0.6, which we designated as hub immune-related genes.

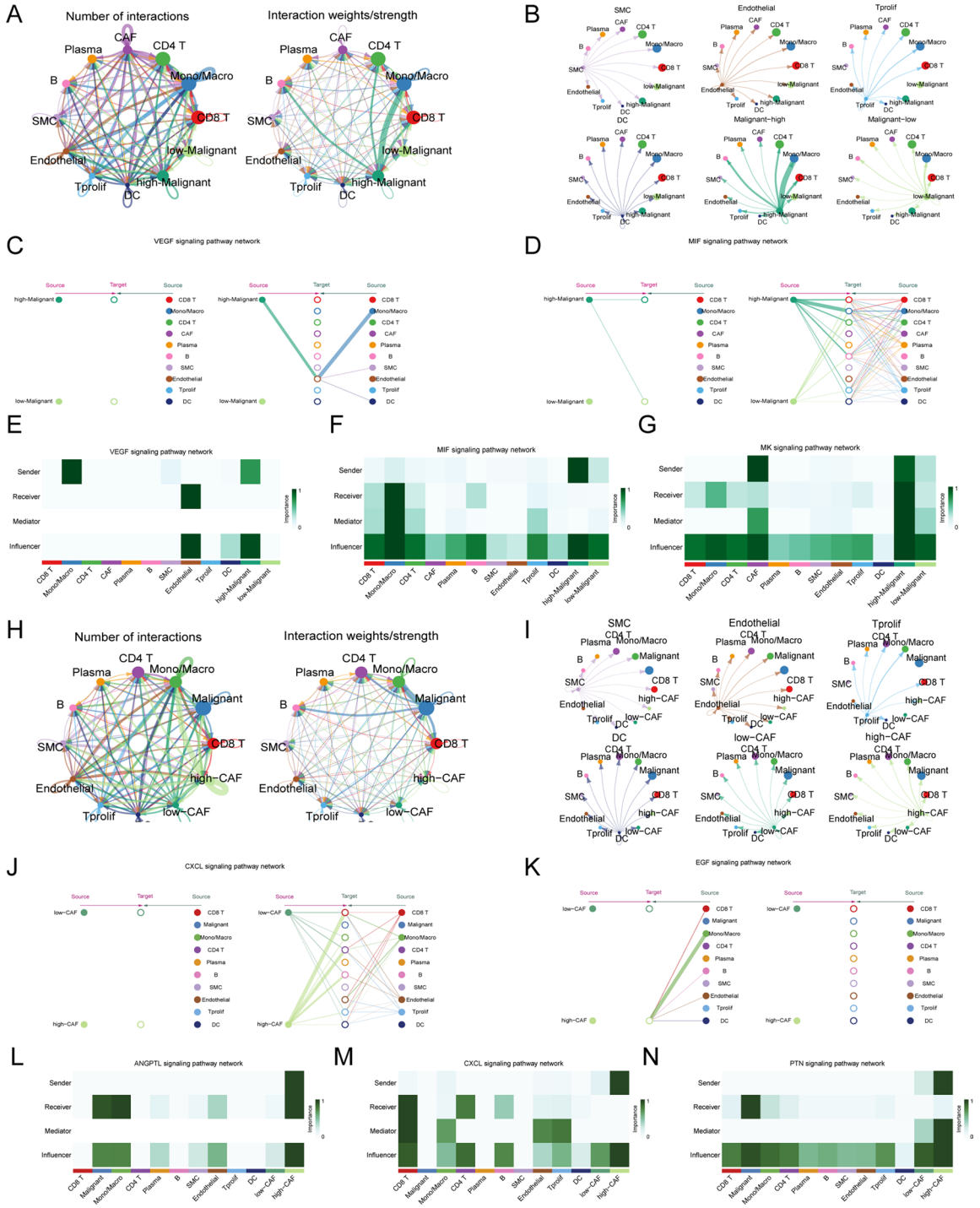

Fig. 4 Cell–cell communication analysis in CAFs and malignant cells with different LPGs scores. **A** Interaction net count plot of other TNBC cells with different scores of Malignant. **B** Communication signals from other TNBC cells with different scores of Malignant. **C** Hierarchical plot of interaction net count plot of other TNBC cells with different scores of Malignant in the VEGF pathway. **D** Hierarchical plot of interaction net count plot of other TNBC cells with different scores of Malignant in the MIF pathway.**E** The VEGF pathway in highly malignant communicates more closely with the TME. **F** The MIF pathway in highly malignant cells communicates more closely with the TME. **G** The MK pathway communicates more closely with the TME. **H** Interaction net count plot of other TNBC cells with different scores of CAFs. **I** Communication signals from other TNBC cells with different scores of CAFs. **G** Hierarchical plot of interaction net count plot of other TNBC cells with different scores of CAFs in the CXCL pathway. **K** Hierarchical plot of interaction net count plot of other TNBC cells with different scores of CAFs in the EGF pathway. **L** The ANGPTL(Angiopoietin-Like Protein) pathway in high-CAF communicate more closely with TME. **M** The CXCL pathway in high-CAF communicate more closely with TME. **N** The PTN pathway in high-CAF communicate more closely with TME

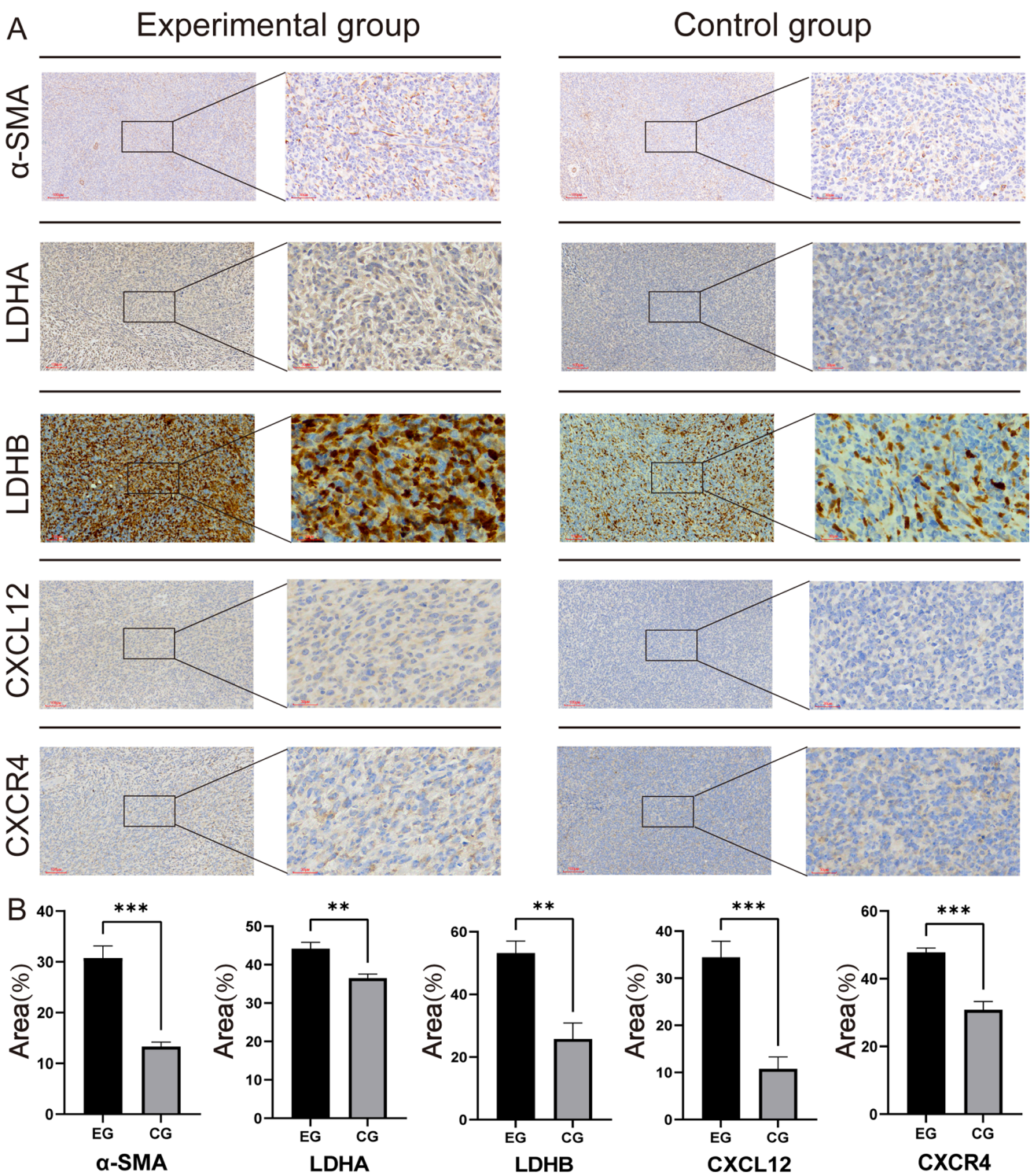

Fig. 5 Immunohistochemical analysis of protein expression in experimental group (EG) and control group (CG). **A** Representative images of immunohistochemical staining for α-SMA (A), LDHA, LDHB,CXCL12, and CXCR4 in EG and CG tissues. Insets show higher magnification views of the respective staining. **B** Quantification of positive staining area (% area) for each marker. Data are expressed as mean ± SEM, and statistical significance was determined using appropriate tests (***$p < 0.005$, **$p < 0.01$). EG, experimental group; CG, control group

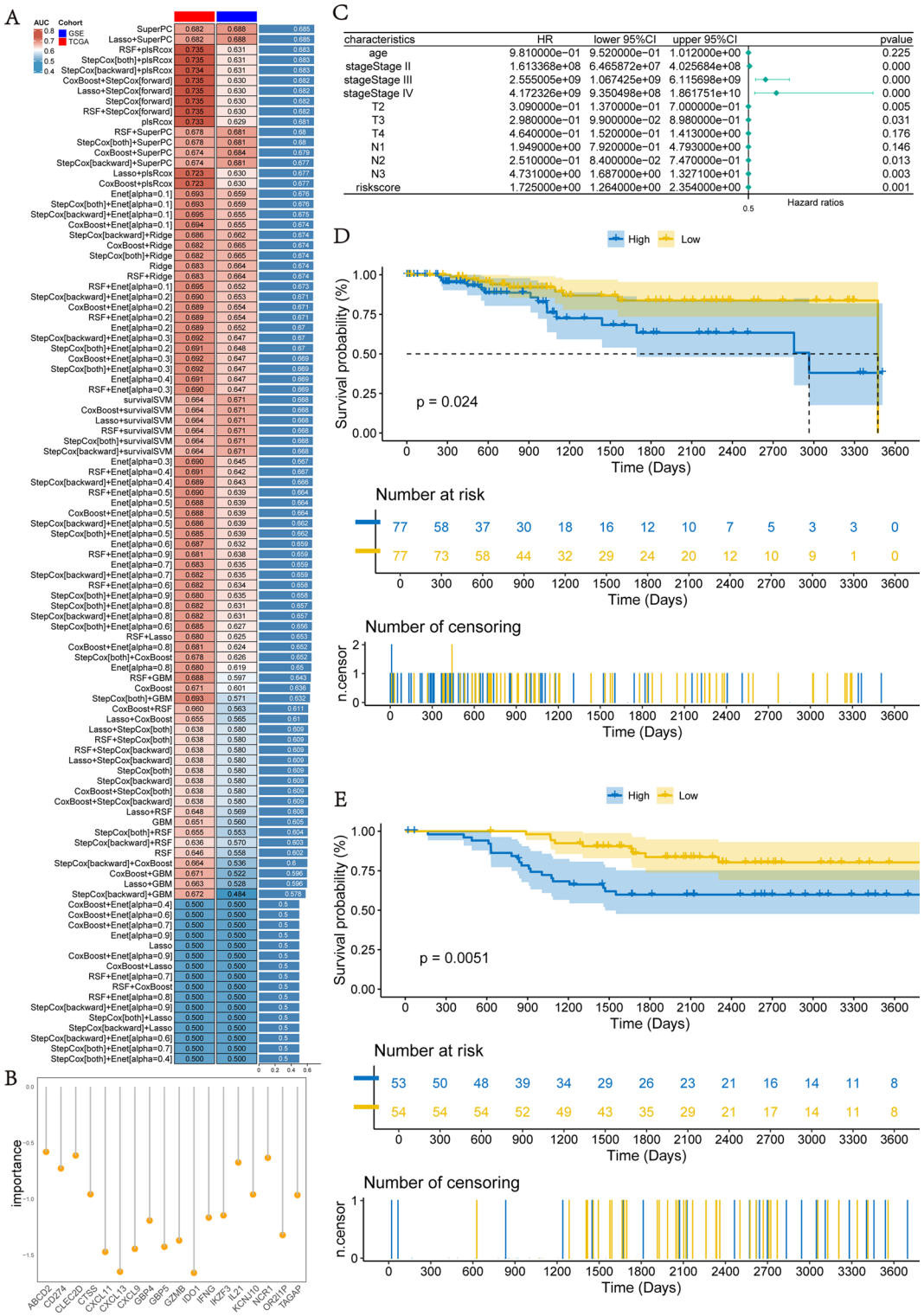

Fig. 6 A consensus LIRGS was developed and validated via machine learning-based integration. **A** A total of 101 versions of prediction models via LOOCV framework and further calculated the C-index of each model across all validation datasets. **B** Importance of 18 genes in LIRGS. **C** Multivariate Cox regression analysis in the TCGA dataset. **D** Kaplan–Meier survival curves clearly demonstrate overall survival rates stratified by LIRGS in patients with TNBC from the TCGA-BRCA dataset. **E** Kaplan–Meier survival curves clearly demonstrate overall survival rates stratified by LIRGS in patients from the GSE58812 dataset

3.6 Integrative consensus signature construction

Based on a set of 324 lactate immunity-related genes, we conducted a univariate Cox analysis. We identified 19 genes that were strongly associated with prognosis ($P < 0.05$). These 19 genes were subjected to machine learning-driven integration. Across both the TCGA and GSE58812 datasets, we constructed 101 prediction models using the LOOCV framework and subsequently evaluated the predictive performance of each model by computing the C-index. The results indicated that the 'Super PC' algorithm achieved the highest average C-index, specifically 0.689 (Fig. 6A). Through 'Super PC,' we derived a risk model, termed the lactate-immune-related gene signature (LIRGS), which consists of 18 genes (Fig. 6B). LIRGS enables the calculation of risk scores tailored to each individual sample. Univariate Cox and multivariate Cox analyses revealed that risk scores could be used as independent prognostic factors to evaluate the survival rates of patients (Fig. 6C).

The 154 patients from the TCGA dataset were stratified based on their risk scores, resulting in two distinct groups: 76 patients in the high-risk category and 76 patients in the low-risk category. Subsequent survival analysis was conducted and Kaplan–Meier survival curves revealed a statistically significant difference in survival outcomes between the high- and low-risk groups (Fig. 6D). To further validate this prognostic model, we applied it to a separate dataset of 107 patients with TNBC from the GSE58812 data set. Survival analysis confirmed a statistically significant prognostic difference between the high- and low-risk groups (Fig. 6E).

LIRGS was used to assess the risk of TNBC across five datasets (TCGA-BRCA, GSE58812, GSE18864, GSE76124, GSE83937), stratifying samples into high- and low-risk groups. Immune cell infiltration was significantly higher in the low-risk group, indicating distinct immunological profiles (Fig.S2). Additionally, the low-risk group exhibited elevated expression of immune checkpoint markers, including PDCD1, PDCD1LG2, LAG3, HAVCR2, CTLA4, CCR4, TIGIT, and CD27, suggesting potential differences in immunotherapy responses (Fig.S3).

4 Discussion

The reprogramming of energy metabolism has emerged as a pivotal aspect among the 14 hallmark traits of cancer, significantly contributing to the formation of a high-lactate environment [46]. Elevated lactate levels promote tumor metastasis, angiogenesis, and immunosuppression. Lactate, once regarded as a metabolic waste product, has evolved into a central figure in the metabolic reprogramming of tumors [47]. It intricately molds the TME and directly influences immune cells [48]. An increasing amount of research effort is now focused on deciphering the complex interplay between lactate and diverse cells within the TME. This line of inquiry holds promise for enhancing the effectiveness of antitumor immunotherapies.

In the intricate milieu of the TME, CAFs, and malignant cells are the primary sources of lactate [43, 44]. Our research indicated a profound connection between these cellular components and lactate metabolism within the TME. Hence, we investigated the biological functions of CAFs and malignant cells under various metabolic paradigms and identified that cells exhibiting elevated lactate metabolism exhibited pronounced immunosuppressive functions within the TME.

Tumor cells engaged in intense glycolysis tend to exhibit greater invasiveness [10]. Our findings further suggest that increased lactate production is not solely correlated with rapid tumor cell proliferation. Tumor cells with elevated lactate output can stimulate the growth of endothelial cells via the VEGF pathway, thereby inducing angiogenesis within the tumor mass. Conversely, cells expressing low levels of lactate genes contribute minimally to this pathway, whereas malignant cells producing high levels of lactate exhibit greater activity in the MIF pathway, particularly through the CD74/CXCR4 and CD74/CD44 signaling axes. These signaling mechanisms regulate mono/macro-immune functions and promote inflammatory responses, ultimately shaping the immunosuppressive TME.

The CXCL12/CXCR4 signaling axis has garnered significant attention due to its role in creating an immunosuppressive tumor microenvironment [49]. Recent studies have demonstrated that in oral squamous cell carcinoma (OSCC), high lactate metabolism promotes the transcription of CXCL12 by enhancing HIF-1α expression in CAFs [50]. This, in turn, leads to increased infiltration of T regulatory (Treg) cells and enhanced secretion of TGF-β, thereby fostering the establishment of an immune-suppressive microenvironment. In our study, we observe that high lactate metabolism similarly promotes the expression of this signaling axis in CAFs within the context of TNBC. This suggests

that targeting CAFs and the CXCL12/CXCR4 signaling axis under conditions of high lactate metabolism may offer a novel immune therapeutic strategy for TNBC patients, particularly those with poor response to immune checkpoint inhibitors.

This study provides valuable insights into the role of lactate metabolism in immune suppression within TNBC, but several limitations must be considered. First, the validation of our prognostic model was based on a limited number of datasets, which may affect its generalizability due to variations in patient characteristics and data processing methods. Second, the lactate metabolism-related genes selected were derived from existing literature and public databases, potentially excluding relevant genes that have not been fully explored. Lastly, while a significant correlation between lactate metabolism and immune suppression was observed, the exact mechanisms remain unclear. Future studies should employ more experimental models to investigate the causal relationship between lactate metabolism and immune responses, which will provide a deeper understanding of its potential as a therapeutic target.

In summary, this study not only enhances our understanding of the underlying mechanisms of lactate function in the TNBC TME, but also lays a robust scientific foundation for the advancement of more potent immunotherapy strategies. Future investigations should delve deeper into targeted interventions for lactate-associated pathways to strive for substantial advancements in TNBC therapeutics.

Acknowledgements We express our gratitude to the Pathology Department of Weifang Traditional Chinese Hospital for their support in our experiments.

Author contributions XHG,CL and THW conceived and designed the study; YL,WFZ and MPZ acquired the data. CGS obtained funding. CDG,YY and RJL did the data analysis and verified the underlying data. All authors drafted the manuscript, revised and approved the final manuscript.

Funding The present study was supported by Grants from the National Natural Science Foundation of China (Grant No. 82305000), the Collaborative Scientific and Technological Project of the Science and Technology Department of the National Administration of Traditional Chinese Medicine (Grant No. GZY-KJS-SD-2023-023), the "Taishan Scholars" Special Foundation of Shandong Province (Grant No. tstp20221166), the Natural Science Foundation of Shandong Province (Grant No. ZR2021LZY015), the Natural Science Foundation of Shandong Province (Grant No. ZR2024QH052), the Youth Innovation Team Development Program for Higher Education Institutions in Shandong Province (Grant No. 2023KJ256), the Traditional Chinese Medicine Science and Technology Project of Shandong Province (Grant No. Q-2023205), and the Qingdao Science and Technology Public-interest Demonstration Project (Grant No. 23-2-8-smjk-1-nsh).

Data availability The data and supporting materials regarding the findings of this study are accessible in the main document as well as in additional information.

Declarations

Ethics approval and consent to participate The study was approved by the Ethics Committee of Shandong Second University of Medicine (Approval No. 2024SDL646). It was conducted in accordance with the guidelines for research involving animal participants established by the Ethics Committee of Shandong Second University of Medicine and in full compliance with the Basel Declaration. All procedures adhered to the ethical standards for animal experimentation.

Consent for publication All authors have read the manuscript and provided their consent for the submission.

Competing interests The authors declare no competing interests.

References

1. Siegel RL, Miller KD, Mbbs NSW, Dvm AJ. Cancer statistics, 2023 2023.
2. Garrido-Castro AC, Lin NU, Polyak K. Insights into molecular classifications of triple-negative breast cancer: improving patient selection for treatment. Cancer Discov. 2019;9:176–98. https://doi.org/10.1158/2159-8290.CD-18-1177.
3. Bianchini G, De Angelis C, Licata L, Gianni L. Treatment landscape of triple-negative breast cancer — expanded options, evolving needs. Nat Rev Clin Oncol. 2022;19:91–113. https://doi.org/10.1038/s41571-021-00565-2.

4. Liu Y, Hu Y, Xue J, Li J, Yi J, Bu J, Zhang Z, Qiu P, Gu X. Advances in immunotherapy for triple- negative breast cancer 2023.
5. Li Y, Zhang H, Merkher Y, Chen L, Liu N, Leonov S, Chen Y. Recent advances in therapeutic strategies for triple-negative breast cancer. J Hematol Oncol. 2022;15:121. https://doi.org/10.1186/s13045-022-01341-0.
6. Keenan TE, Tolaney SM. Role of immunotherapy in triple-negative breast cancer. J Natl Compr Canc Netw. 2020;18:479–89. https://doi.org/10.6004/jnccn.2020.7554.
7. Pitt JM, Marabelle A, Eggermont A, Soria J-C, Kroemer G, Zitvogel L. Targeting the tumor microenvironment: removing obstruction to anticancer immune responses and immunotherapy. Ann Oncol. 2016;27:1482–92. https://doi.org/10.1093/annonc/mdw168.
8. Hanahan D, Weinberg RA. Hallmarks of cancer: the next generation. Cell. 2011;144:646–74. https://doi.org/10.1016/j.cell.2011.02.013.
9. Schmidt DR, Patel R, Kirsch DG, Lewis CA, Vander Heiden MG, Locasale JW. Metabolomics in cancer research and emerging applications in clinical oncology. CA A Cancer J Clinicians. 2021;71:333–58. https://doi.org/10.3322/caac.21670.
10. Jing X, Yang F, Shao C, Wei K, Xie M, Shen H, Shu Y. Role of hypoxia in cancer therapy by regulating the tumor microenvironment. Mol Cancer. 2019;18:157. https://doi.org/10.1186/s12943-019-1089-9.
11. Brooks GA. The science and translation of lactate shuttle theory. Cell Metab. 2018;27:757–85. https://doi.org/10.1016/j.cmet.2018.03.008.
12. Heiden MGV, Cantley LC, Thompson CB. Understanding the Warburg Effect: The Metabolic Requirements of Cell Proliferation 2010.
13. Koppenol WH, Bounds PL, Dang CV. Otto Warburg's contributions to current concepts of cancer metabolism. Nat Rev Cancer. 2011;11:325–37. https://doi.org/10.1038/nrc3038.
14. Sebestyén A. Tumor metabolism: metabolic alterations and heterogeneity in cancer progression. Cancer Metastasis Rev. 2021;40:987–8. https://doi.org/10.1007/s10555-021-10008-0.
15. Apostolova P, Pearce EL. Lactic acid and lactate: revisiting the physiological roles in the tumor microenvironment. Trends Immunol. 2022;43:969–77. https://doi.org/10.1016/j.it.2022.10.005.
16. Dai E, Wang W, Li Y, Ye D, Li Y. Lactate and lactylation: Behind the development of tumors. Cancer Lett. 2024;591: 216896. https://doi.org/10.1016/j.canlet.2024.216896.
17. Li X. Lactate metabolism in human health and disease. Signal Transduction and Targeted Therapy. 2022.
18. Certo M. Lactate modulation of immune responses in inflammatory versus tumour microenvironments n.d.
19. Watson MJ, Delgoffe GM. Fighting in a wasteland: deleterious metabolites and antitumor immunity. J Clin Investig. 2022;132: e148549. https://doi.org/10.1172/JCI148549.
20. Xu J, Shen H, Zhu Z, Tang J. Lactate-induced lactylation circularly regulates glucose metabolism enzymes in breast cancer. JCO. 2023;41:e13092–e13092. https://doi.org/10.1200/JCO.2023.41.16_suppl.e13092.
21. Cappelletti V, Iorio E, Miodini P, Silvestri M, Dugo M, Daidone MG. Metabolic Footprints and Molecular Subtypes in Breast Cancer. Disease Markers.
22. Choi SYC, Collins CC, Gout PW, Wang Y. Cancer-generated lactic acid: a regulatory, immunosuppressive metabolite? J Pathol. 2013;230:350–5. https://doi.org/10.1002/path.4218.
23. Hu X, Chao M, Wu H. Central role of lactate and proton in cancer cell resistance to glucose deprivation and its clinical translation. Sig Transduct Target Ther. 2017;2:16047. https://doi.org/10.1038/sigtrans.2016.47.
24. Dhup S, Kumar Dadhich R, Ettore Porporato P, Sonveaux P. Multiple biological activities of lactic acid in cancer: influences on tumor growth. Angiogenesis and Metastasis CPD. 2012;18:1319–30. https://doi.org/10.2174/138161212799504902.
25. Caslin H, Abebayehu D, Qayum AA, Hoeferlin LA, Chalfant CE, Ryan JJ. Lactic acid suppresses LPS-induced cytokine production in vitro and in vivo. J Immunol. 2017;198:222. https://doi.org/10.4049/jimmunol.198.Supp.222.16.
26. Türkcan S, Kiru L, Naczynski DJ, Sasportas LS, Pratx G. Lactic Acid Accumulation in the Tumor Microenvironment Suppresses 18F-FDG Uptake. Can Res. 2019;79:410–9. https://doi.org/10.1158/0008-5472.CAN-17-0492.
27. Jiang K, Zhu L, Huang H, Zheng L, Wang Z, Kang X. Lactate score classification of hepatocellular carcinoma helps identify patients with tumors that respond to immune checkpoint blockade therapy. Cell Oncol. 2024;47:175–88. https://doi.org/10.1007/s13402-023-00861-2.
28. Wilkerson MD, Hayes DN. ConsensusClusterPlus: a class discovery tool with confidence assessments and item tracking. Bioinformatics. 2010;26:1572–3. https://doi.org/10.1093/bioinformatics/btq170.
29. Şenbabaoğlu Y, Michailidis G, Li JZ. Critical limitations of consensus clustering in class discovery. Sci Rep. 2014;4:6207. https://doi.org/10.1038/srep06207.
30. Wu J, Li L, Zhang H, Zhao Y, Zhang H, Wu S, Xu B. A risk model developed based on tumor microenvironment predicts overall survival and associates with tumor immunity of patients with lung adenocarcinoma. Oncogene. 2021;40:4413–24. https://doi.org/10.1038/s41388-021-01853-y.
31. Chen Y, Feng Y, Yan F, Zhao Y, Zhao H, Guo Y. A novel immune-related gene signature to identify the tumor microenvironment and prognose disease among patients with oral squamous cell carcinoma patients using ssGSEA: a bioinformatics and biological validation study. Front Immunol. 2022;13: 922195. https://doi.org/10.3389/fimmu.2022.922195.
32. Wu T, Hu E, Xu S, Chen M, Guo P, Dai Z, Feng T, Zhou L, Tang W, Zhan L, Fu X, Liu S, Bo X, Yu G. clusterProfiler 4.0: A universal enrichment tool for interpreting omics data. Innovation. 2021;2:100141. https://doi.org/10.1016/j.xinn.2021.100141.
33. Lee MYY, Kaestner KH, Li M. Benchmarking algorithms for joint integration of unpaired and paired single-cell RNA-seq and ATAC-seq data. Genome Biol. 2023;24:244. https://doi.org/10.1186/s13059-023-03073-x.
34. Han Y, Wang Y, Dong X, Sun D, Liu Z, Yue J, Wang H, Li T, Wang C. TISCH2: expanded datasets and new tools for single-cell transcriptome analyses of the tumor microenvironment. Nucleic Acids Res. 2023;51:D1425–31. https://doi.org/10.1093/nar/gkac959.
35. He L, Fan Y, Zhang Y, Tu T, Zhang Q, Yuan F, Cheng C. Single-cell transcriptomic analysis reveals circadian rhythm disruption associated with poor prognosis and drug-resistance in lung adenocarcinoma. J Pineal Res. 2022;73: e12803. https://doi.org/10.1111/jpi.12803.
36. Wei W, Liu Y, Shen Y, Yang T, Dong Y, Han Z, Wang Y, Liu Z, Chai Y, Zhang M, Wang H, Shen H, Shen Y, Chen M. In situ tissue profile of rat trigeminal nerve in trigeminal neuralgia using spatial transcriptome sequencing. Int J Surg. 2024;110:1463–74. https://doi.org/10.1097/JS9.0000000000001110.
37. Liu Z, Sun D, Wang C. Evaluation of cell-cell interaction methods by integrating single-cell RNA sequencing data with spatial information. Genome Biol. 2022;23:218. https://doi.org/10.1186/s13059-022-02783-y.

38. Ford K, Hanley CJ, Mellone M, Szyndralewiez C, Heitz F, Wiesel P, et al. NOX4 inhibition potentiates immunotherapy by overcoming cancer-associated fibroblast-mediated CD8 T-cell exclusion from tumors. Can Res. 2020;80:1846–60. https://doi.org/10.1158/0008-5472.CAN-19-3158.
39. Xu M, Zhou H, Hu P, Pan Y, Wang S, Liu L, Liu X. Identification and validation of immune and oxidative stress-related diagnostic markers for diabetic nephropathy by WGCNA and machine learning. Front Immunol. 2023;14:1084531. https://doi.org/10.3389/fimmu.2023.1084531.
40. Liu Z, Liu L, Weng S, Guo C, Dang Q, Xu H, Wang L, Lu T, Zhang Y, Sun Z, Han X. Machine learning-based integration develops an immune-derived lncRNA signature for improving outcomes in colorectal cancer. Nat Commun. 2022;13:816. https://doi.org/10.1038/s41467-022-28421-6.
41. Green AR. MYC functions are specific in biological subtypes of breast cancer and confers resistance to endocrine therapy in luminal tumours. British J Cancer.
42. Pandkar MR. Oncometabolite lactate enhances breast cancer progression by orchestrating histone lactylation-dependent c-Myc expression. Translational Oncology. 2023.
43. Wang Z-H. Lactate in the tumour microenvironment: From immune modulation to therapy 2021.
44. Frisardi V, Canovi S, Vaccaro S, Frazzi R. The significance of microenvironmental and circulating lactate in breast cancer. IJMS. 2023;24:15369. https://doi.org/10.3390/ijms242015369.
45. Piersma B, Hayward M-K, Weaver VM. Fibrosis and cancer: A strained relationship. Rev Cancer. 2020;1873:188356. https://doi.org/10.1016/j.bbcan.2020.188356.
46. Hanahan D. Hallmarks of Cancer: New Dimensions. Cancer Discov. 2022;12:31–46. https://doi.org/10.1158/2159-8290.CD-21-1059.
47. Ippolito L. Lactate: A Metabolic Driver in the Tumour Landscape.
48. Zha J, Zhang J, Lu J, Zhang G, Hua M, Guo W, Yang J, Fan G. A review of lactate-lactylation in malignancy: its potential in immunotherapy. Front Immunol. 2024;15:1384948. https://doi.org/10.3389/fimmu.2024.1384948.
49. Yang Y, Li J, Lei W, Wang H, Ni Y, Liu Y, Yan H, Tian Y, Wang Z, Yang Z, Yang S, Yang Y, Wang Q. CXCL12-CXCR4/CXCR7 Axis in Cancer: from Mechanisms to Clinical Applications. Int J Biol Sci. 2023;19:3341–59. https://doi.org/10.7150/ijbs.82317.
50. Liu Z, Zhang Z, Zhang Y, Zhou W, Zhang X, Peng C, Ji T, Zou X, Zhang Z, Ren Z. Spatial transcriptomics reveals that metabolic characteristics define the tumor immunosuppression microenvironment via iCAF transformation in oral squamous cell carcinoma. Int J Oral Sci. 2024;16:9. https://doi.org/10.1038/s41368-023-00267-8.